

# Local real space operators for translating Stokes Q/U to E/B maps on the sphere

**Aditya Rotti and Kevin Huffenberger**

Department of Physics, Florida State University, Keen Physics Building, 77 Chieftan Way, Tallahassee, Florida, U.S.A.

E-mail: [adityarotti@gmail.com](mailto:adityarotti@gmail.com), [khuffenberger@fsu.edu](mailto:khuffenberger@fsu.edu)

**Abstract.** We derive real space operators to translate Stokes Q/U to coordinate independent even and odd parity E/B fields on the sphere and demonstrate their numerical equivalence to the harmonic space methods. In process we also derive real space operators which allow direct decomposition of measured Q/U into Q/U fields corresponding to E-modes and B-modes respectively. These operators are derived on the sphere and account for the curvature effects. The analytical derivations reveal a functional form for the radial kernel, which quantifies the non-local nature of the E and B fields. These real space operators allow the computation of E and B field in each pixel by integrating in a small region around it, and hence it can be easily parallelized and is not memory intensive. A major drawback of these real space operators is that they cannot reliably construct modes on large angular scales  $\ell < 50$  with ease. Finally, this study motivates the construction of more locally defined E and B maps, by making desired alterations to the radial filter. We demonstrate that these altered E mode and B mode constructions do not significantly distort spectral information on small angular scales.

---

## Contents

<b>1</b>	<b>Introduction</b>	<b>2</b>
<b>2</b>	<b>E/B description of CMB polarization</b>	<b>3</b>
2.1	Polarization primer	3
2.2	Matrix notation	4
<b>3</b>	<b>Real space operators</b>	<b>5</b>
3.1	Evaluating E & B fields from measured Stokes parameters Q & U	5
3.2	Evaluating Stokes parameters Q & U fields from E & B fields	7
3.3	Decomposing Q & U Stokes parameters into those corresponding to E & B modes respectively	8
3.4	Visualizing the convolution kernels	10
3.5	Quantifying the non-locality of E & B modes	12
<b>4</b>	<b>Numerical implementation</b>	<b>14</b>
4.1	Constructing E & B maps using local convolutions	14
4.2	Separating Stokes Q & U maps corresponding to E & B modes of polarization	17
4.3	Multipole filtering using spatial convolutions	19
4.4	Application to Planck 353 Ghz polarization maps	22
4.5	Scaling and future prospects	22
<b>5</b>	<b>Discussion</b>	<b>24</b>
<b>6</b>	<b>Appendix</b>	<b>26</b>
6.1	Mathematical properties of spin spherical harmonics	26
6.2	Asymptotic forms for the functions $\pm_2 f_\ell(\beta)$	26
6.3	Convolution error	27
6.4	The correlation function and radial cut offs.	28

---

## 1 Introduction

In this work we follow the convention in which bar-ed variables correspond to those in real space, while the tilde-ed variables correspond to those in harmonic space [1].

This paper is organized in the following manner: In Sec. 2 we present a primer on the description of CMB polarization on the sphere and introduce the matrix notation which provides a more concise description of the same. In Sec. 3 we introduce the necessary tools and discuss the derivations of the real space operators. In Sec. 3.4 we evaluate the real space operators and present visualizations of these functions. Here we discuss the locality of the real space E & B operators. In Sec. 4 we implement these operators to evaluate E & B maps from the Stokes parameters Q & U and compare these maps and their spectra from those derived using Healpix. We conclude with a discussion and the scope of this new method of analyzing CMB polarization in Sec. 5.

## 2 E/B description of CMB polarization

### 2.1 Polarization primer

The CMB polarization is measured in terms of Stokes Q and U parameters. These measurements can be combined to form the complex spin 2 polarization field as follows,

$$\begin{aligned}\pm_2 \bar{X}(\hat{n}) &= Q(\hat{n}) \pm iU(\hat{n}) \\ &= \sum_{\ell m} \pm_2 \tilde{X}_{\ell m} \pm_2 Y_{\ell m}(\hat{n}).\end{aligned}\quad (2.1)$$

Since these measured quantities depend on the local coordinate system making it is cumbersome to work with them. To overcome this, one describes the CMB polarization field in terms of a scalar field denoted by  $E(\hat{n})$  and a pseudo scalar field  $B(\hat{n})$  [2]. These scalar fields are related to the spin-2 polarization field  $\pm_2 X(\hat{n})$  through the following relation,

$$\mathcal{E}(\hat{n}) = -\frac{1}{2} [\bar{\partial}_{+2}^2 X(\hat{n}) + \bar{\partial}_{-2}^2 X(\hat{n})] ; \mathcal{B}(\hat{n}) = -\frac{1}{2i} [\bar{\partial}_{+2}^2 X(\hat{n}) - \bar{\partial}_{-2}^2 X(\hat{n})], \quad (2.2)$$

where  $\bar{\partial}$  and  $\bar{\partial}$  denote the spin raising and lowering operators respectively. These  $E$  and  $B$  fields are spin-0 fields similar to the temperature anisotropies and hence their value are independent of the coordinate system definitions. The spin raising and lowering operators have the following properties [3],

$$\bar{\partial}_s Y_{lm}(\hat{n}) = \sqrt{(\ell-s)(\ell+s+1)} {}_{s+1} Y_{lm}(\hat{n}), \quad (2.3a)$$

$$\bar{\partial}_s Y_{lm}(\hat{n}) = -\sqrt{(\ell+s)(\ell-s+1)} {}_{s-1} Y_{lm}(\hat{n}), \quad (2.3b)$$

where  ${}_s Y_{lm}(\hat{n})$  denote the spin-s spherical harmonics.

Using Eq. (2.2) and the properties of the spin raising and lowering operators given in Eq. (2.3a) it can be shown that the scalar fields  $\mathcal{E}/\mathcal{B}$  are defined via the following set of equations,

$$\mathcal{E}(\hat{n}) = \sum_{\ell m} a_{\ell m}^E \sqrt{\frac{(\ell+2)!}{(\ell-2)!}} Y_{\ell m}(\hat{n}) ; \mathcal{B}(\hat{n}) = \sum_{\ell m} a_{\ell m}^B \sqrt{\frac{(\ell+2)!}{(\ell-2)!}} Y_{\ell m}(\hat{n}), \quad (2.4)$$

where the harmonic coefficients of  $\mathcal{E}/\mathcal{B}$  fields are related to the spin harmonic coefficients of the polarization field through the following equations,

$$a_{\ell m}^E = -\frac{1}{2} \left[ {}_{+2} X_{\ell m} + {}_{-2} X_{\ell m} \right] ; a_{\ell m}^B = -\frac{1}{2i} \left[ {}_{+2} X_{\ell m} - {}_{-2} X_{\ell m} \right] \quad (2.5)$$

In the remainder of this article, we will work with the scalar  $E$  and pseudo scalar  $B$  fields as defined by the following expressions,

$$E(\hat{n}) = \sum_{\ell m} a_{\ell m}^E Y_{\ell m}(\hat{n}) ; B(\hat{n}) = \sum_{\ell m} a_{\ell m}^B Y_{\ell m}(\hat{n}). \quad (2.6)$$

Note that the two set of fields  $\mathcal{E}/\mathcal{B}$  and  $E/B$  differ, since their spherical harmonic coefficients of expansion differ by the factor of  $\sqrt{\frac{(\ell+2)!}{(\ell-2)!}}$ .

## 2.2 Matrix notation

In this section we cast the relation introduced in Sec. 2.1 in matrix notation<sup>1</sup>. This representation will make transparent the derivation of the real space operators we discuss in the following sections. We adopt a convention in which real space quantities are denoted by bar-ed variable while those in harmonic space are denoted by tilde-ed variables.

We begin by introducing the matrices encoding the spin spherical harmonic basis vectors,

$${}_sB = \begin{bmatrix} {}^{+s}Y & 0 \\ 0 & {}^{-s}Y \end{bmatrix}_{2N_{\text{pix}} \times 2N_{\text{alms}}}, \quad (2.7)$$

where  $s$  denotes the spin of the basis functions. For this work we will only be working with cases  $s \in [0, 2]$ . In this notation, each column can be mapped to a specific harmonic basis function marked by the pair of indices:  $(\ell, m)$  and each row maps to a specific position on the sphere. Note that this matrix is in general not a square matrix. Generally the number of columns is determined by the scheme used to discretely represent the sphere and the number of rows is set by the number of basis functions of interest (often determined the band limit).

We now define the different data vectors and their representation in real and harmonic space as follows,

$$\bar{S} = \begin{bmatrix} E \\ B \end{bmatrix}_{2N_{\text{pix}} \times 1} ; \quad \bar{X} = \begin{bmatrix} {}^{+2}X \\ {}^{-2}X \end{bmatrix}_{2N_{\text{pix}} \times 1} ; \quad \bar{P} = \begin{bmatrix} Q \\ U \end{bmatrix}_{2N_{\text{pix}} \times 1}, \quad (2.8a)$$

$$\tilde{S} = \begin{bmatrix} a^E \\ a^B \end{bmatrix}_{2N_{\text{alms}} \times 1} ; \quad \tilde{X} = \begin{bmatrix} {}^{+2}\tilde{X} \\ {}^{-2}\tilde{X} \end{bmatrix}_{2N_{\text{alms}} \times 1}. \quad (2.8b)$$

The different symbols have the same meaning as that discussed in Sec. 2.1, except that the subscript  $\ell_m$  for the spherical harmonic coefficients of expansion is suppressed to avoid clutter in notation.

Next we define the operators which govern the transformations between different representations of the polarization field as follows,

$$\bar{T} = \begin{bmatrix} 1 & i\mathbb{1} \\ \mathbb{1} & -i\mathbb{1} \end{bmatrix}_{2N_{\text{pix}} \times 2N_{\text{pix}}} ; \quad \bar{T}^{-1} = \frac{1}{2}\bar{T}^\dagger, \quad (2.9a)$$

$$\tilde{T} = -\begin{bmatrix} 1 & i\mathbb{1} \\ \mathbb{1} & -i\mathbb{1} \end{bmatrix}_{2N_{\text{alms}} \times 2N_{\text{alms}}} ; \quad \tilde{T}^{-1} = \frac{1}{2}\tilde{T}^\dagger. \quad (2.9b)$$

Using the data vectors and the all the operators defined in this section we now write down, in compact notation, the forward and inverse relations between different representations of the polarization field as follows,

$$\bar{X} = \bar{T} * \bar{P} ; \quad \bar{P} = \frac{1}{2}\bar{T}^\dagger * \bar{X}, \quad (2.10a)$$

$$\bar{X} = {}_2B * \tilde{X} ; \quad \tilde{X} = {}_2B^\dagger * \bar{X}, \quad (2.10b)$$

$$\tilde{X} = \tilde{T} * \tilde{S} ; \quad \tilde{S} = \frac{1}{2}\tilde{T}^\dagger * \tilde{X}. \quad (2.10c)$$

$$\bar{S} = {}_0B * \tilde{S} ; \quad \tilde{S} = {}_0B^\dagger * \bar{S}. \quad (2.10d)$$

---

<sup>1</sup>While we work with the matrix and vector sizes given in terms of Healpix pixelization parameter  $N_{\text{pix}}$ , all the relations are equally valid in the continuum limit attained by allowing  $N_{\text{pix}} \rightarrow \infty$

Next we introduce the harmonic space operators, which project the harmonic space data vector to E or B subspace,

$$\tilde{O}_E = \begin{bmatrix} 1 & 0 \\ 0 & 0 \end{bmatrix}_{2N_{\text{alms}} \times 2N_{\text{alms}}} ; \quad \tilde{S}_E = \tilde{O}_E * \tilde{S}, \quad (2.11a)$$

$$\tilde{O}_B = \begin{bmatrix} 0 & 0 \\ 0 & 1 \end{bmatrix}_{2N_{\text{alms}} \times 2N_{\text{alms}}} ; \quad \tilde{S}_B = \tilde{O}_B * \tilde{S}. \quad (2.11b)$$

Note that these harmonic space matrices are idempotent, orthogonal to each other and their sum is an identity matrix as can be explicitly seen via the following relations,

$$\tilde{O}_E * \tilde{O}_E = \tilde{O}_E ; \quad \tilde{O}_B * \tilde{O}_B = \tilde{O}_B, \quad (2.12a)$$

$$\tilde{O}_E * \tilde{O}_B = \emptyset, \quad (2.12b)$$

$$\tilde{O}_E + \tilde{O}_B = \mathbb{1}. \quad (2.12c)$$

Here it is important to note that these relations are exact in harmonic space. **In the following sections our aim is to derive real space analogues of these harmonic space operators.**

### 3 Real space operators

In this section we derive the real space operators which translate the Stokes parameters Q & U to E & B fields and vice versa. We also derive real space operators for directly (without first evaluating the E & B field themselves) decomposing the Stokes parameters Q & U in to Stokes parameters that correspond to the E & B fields respectively. We extensively make use of the matrix notation introduced in Sec. 2.2 for these derivations.

All the results are most conveniently expressed as functions of the Euler angles  $\alpha$ ,  $\beta$  &  $\gamma$  on the sphere. Generically, the Euler angles define the rotations that transforms the local cartesian coordinate system defined at the sphere position  $\hat{n}_i \equiv (\theta_i, \phi_i)$  such that it aligns with the local cartesian coordinate system at the location  $\hat{n}_j \equiv (\theta_j, \phi_j)$  [4]. The Euler angles can be evaluated as the following functions of the angular coordinates of the points  $\hat{n}_i \equiv (\theta_i, \phi_i)$  and  $\hat{n}_j \equiv (\theta_j, \phi_j)$ ,

$$\cos(\beta) = \sin(\theta_i) \sin(\theta_j) \cos(\phi_i - \phi_j) + \cos(\theta_i) \cos(\theta_j), \quad (3.1a)$$

$$\tan(\alpha) = \frac{\sin(\phi_i - \phi_j) \sin(\theta_i) \sin(\theta_j)}{\cos(\theta_i) \cos(\beta) - \cos(\theta_j)}, \quad (3.1b)$$

$$\tan(\gamma) = \frac{\sin(\phi_i - \phi_j) \sin(\theta_i) \sin(\theta_j)}{\cos(\theta_j) \cos(\beta) - \cos(\theta_i)}, \quad (3.1c)$$

where  $\beta$  denotes the angular distance between the two points  $\hat{n}_i$  &  $\hat{n}_j$  on the sphere, while the angles  $\alpha$  &  $\gamma$  define rotations which co-align the coordinate axes of the two local coordinate systems. While evaluating the above functions we follow the convention that  $\beta$  lies in the domain  $[0, \pi]$  and that the angles  $\alpha$  &  $\gamma$  lie in the domain  $[-\pi, \pi]$ . It is important to assign the proper signs to  $\alpha$  &  $\gamma$  by duly accounting for the signs of the terms in the numerator and the denominator.

#### 3.1 Evaluating E & B fields from measured Stokes parameters Q & U

In Sec. 2.1 we discussed how the scalar fields E & B are derived from the Stokes parameters Q & U. To reiterate, this process involved taking the spin harmonic transform of the complex spin-2 field ( $\pm_2 \bar{X}$ ), taking linear combinations of the resultant coefficients of expansion

$(\pm_2 \tilde{X}_{\ell m})$  and evaluating the forward spin-0 transform to derive the scalar E & B fields. Here we derive the real space convolution kernels on the sphere which can be used to directly evaluate the scalar E & B fields on the sphere. We use the relations given in Eq. (2.10a), to write down an equation relating the real space vector of scalars  $\bar{S}^\dagger = [E, B]$  to the polarization vector  $\bar{P}^\dagger = [Q, U]$  as given below,

$$\bar{S} = {}_0B * \tilde{T}^{-1} * {}_2B^\dagger * \bar{T} * \bar{P} = \frac{1}{2} {}_0B * \tilde{T}^\dagger {}_2B^\dagger * \bar{T} * \bar{P}, \quad (3.2a)$$

$$= \bar{O} * \bar{P}. \quad (3.2b)$$

The explicit form of the real space operator  $\bar{O}$  can be derived by contracting over all the matrix operators. This procedure of contracting over the operators is explicitly worked out in the following set of equations,

$$\bar{O} = \frac{1}{2} {}_0B * \tilde{T}^\dagger * {}_2B^\dagger * \bar{T}, \quad (3.3a)$$

$$= -0.5 \begin{bmatrix} {}_0Y_i & 0 \\ 0 & {}_0Y_i \end{bmatrix} \begin{bmatrix} \mathbb{1} & \mathbb{1} \\ -i\mathbb{1} & i\mathbb{1} \end{bmatrix} \begin{bmatrix} {}_{+2}Y_j^{T*} & 0 \\ 0 & {}_{-2}Y_j^{T*} \end{bmatrix} \begin{bmatrix} \mathbb{1} & i\mathbb{1} \\ \mathbb{1} & -i\mathbb{1} \end{bmatrix}, \quad (3.3b)$$

$$= -0.5 \begin{bmatrix} \sum({}_0Y_i {}_{+2}Y_j^{T*} + {}_0Y_i {}_{-2}Y_j^{T*}) & i\sum({}_0Y_i {}_{+2}Y_j^{T*} - {}_0Y_i {}_{-2}Y_j^{T*}) \\ -i\sum({}_0Y_i {}_{+2}Y_j^{T*} - {}_0Y_i {}_{-2}Y_j^{T*}) & \sum({}_0Y_i {}_{+2}Y_j^{T*} + {}_0Y_i {}_{-2}Y_j^{T*}) \end{bmatrix}, \quad (3.3c)$$

where the symbol  ${}_0Y_i$  is used to denote the matrix  ${}_0Y_{\hat{n}_i \times \ell m} \equiv {}_0Y_{\ell m}(\hat{n}_i)$ , the symbol  ${}_{\pm 2}Y_j^{T*}$  is used to denote the matrix  ${}_{\pm 2}Y_{\ell m \times \hat{n}_j}^* \equiv {}_{\pm 2}Y_{\ell m}^*(\hat{n}_j)$  and the summation is over the multipole indices  $\ell, m$ . Using the conjugation properties of the spin spherical harmonic functions it can be shown that the following relation holds true,

$$\left[ \sum_{\ell m} {}_0Y_{\ell m}(\hat{n}_i) {}_{+2}Y_{\ell m}^*(\hat{n}_j) \right]^* = \sum_{\ell m} {}_0Y_{\ell m}(\hat{n}_i) {}_{-2}Y_{\ell m}^*(\hat{n}_j). \quad (3.4)$$

where the terms on either side of the equation are those that appear in Eq. (3.3c). Therefore the different parts of the real space operators are completely specified in terms of the complex function,

$$\begin{aligned} \mathcal{M}(\hat{n}_i, \hat{n}_j) &= \mathcal{M}_r + i\mathcal{M}_i, \\ &= \sum_{\ell m} {}_0Y_{\ell m}(\hat{n}_i) {}_{+2}Y_{\ell m}^*(\hat{n}_j) = \sum_{\ell} \sqrt{\frac{2\ell+1}{4\pi}} {}_0Y_{\ell 2}^*(\beta_{ij}, \alpha_{ij}), \end{aligned} \quad (3.5a)$$

$$= \left[ \cos(2\alpha_{ij}) - i \sin(2\alpha_{ij}) \right] \sum_{\ell=\ell_{\min}}^{\ell_{\max}} \frac{2\ell+1}{4\pi} \sqrt{\frac{(\ell-2)!}{(\ell+2)!}} P_{\ell 2}(\cos \beta_{ij}), \quad (3.5b)$$

$$= \left[ \cos(2\alpha_{ij}) - i \sin(2\alpha_{ij}) \right] f(\beta_{ij}, \ell_{\min}, \ell_{\max}), \quad (3.5c)$$

where we have used the property of summation over spin spherical harmonics (see Eq. (6.1)) listed in Appendix 6.1. Here we first note that this function does not depend on the Euler angle  $\gamma$ . This function has a part which depends only on the Euler angle  $\alpha$  and this part of the function has no multipole dependence. except the factor of 2 which arises because the polarization field is a spin-2 field. The other part of the function  $f(\beta, \ell_{\min}, \ell_{\max})$  depends only on the Euler angle  $\beta$  and completely incorporates the multipole dependence of the function.

$f(\beta, \ell_{\min}, \ell_{\max})$  will be often referred to as the radial kernel. The radial kernel is what determines the locality of the operator which translates the Stokes parameters  $Q$  &  $U$  to the scalars  $E$  &  $B$ .

Finally the real space operator can be cast in this simple form,

$$\bar{O} = \begin{bmatrix} -\mathcal{M}_r & -\mathcal{M}_i \\ \mathcal{M}_i & -\mathcal{M}_r \end{bmatrix}_{2N_{\text{pix}} \times 2N_{\text{pix}}} = -f(\beta_{ij}, \ell_{\min}, \ell_{\max}) \begin{bmatrix} \cos(2\alpha_{ij}) & \sin(2\alpha_{ij}) \\ -\sin(2\alpha_{ij}) & \cos(2\alpha_{ij}) \end{bmatrix}, \quad (3.6)$$

where  $i,j$  indices map to the location  $\hat{n}_i$  and  $\hat{n}_j$  on the sphere. A similar equation for real space  $E$  &  $B$  operators was derived in [1], however those results are derived for the flat sky case and do not explicitly derive the radial kernel.  $\Rightarrow$  Maybe a discussion on this should be in the conclusions.

The scalar fields  $E$  &  $B$  can now be directly derived from the measured Stokes  $Q$  &  $U$  parameters by evaluating the following expression,

$$\begin{bmatrix} E_i \\ B_i \end{bmatrix} = -f(\beta_{ij}, \ell_{\min}, \ell_{\max}) \begin{bmatrix} \cos(2\alpha_{ij}) & \sin(2\alpha_{ij}) \\ -\sin(2\alpha_{ij}) & \cos(2\alpha_{ij}) \end{bmatrix} \begin{bmatrix} Q_j \\ U_j \end{bmatrix} \Delta\Omega, \quad (3.7)$$

where we have used the Einstein summation convention: repeated indices are summed over. The factor  $\Delta\Omega$  accounts for the finite pixel size and is important for proper normalization. This has an elegant interpretation: to derive the  $E$  and/or  $B$  field at any given position we need to find the cosine quadrupole transform and the sine quadrupole transform of the Stokes  $Q$  &  $U$  parameters on circles around this position, weigh the transform by the value of the function  $f(\beta, \ell_{\min}, \ell_{\max})$ ,  $\beta$  being the radius of the circle and sum up the results with appropriate signs, to construct the respective scalar fields. While the azimuthal operations do not depend on the choice of basis functions, the radial kernel is completely determined by the choice of the basis functions. One can now think of constructing alternate basis functions which have different radial fall off.

### 3.2 Evaluating Stokes parameters $Q$ & $U$ fields from $E$ & $B$ fields

The real space operator which translates  $E$  &  $B$  fields to Stokes parameters  $Q$  &  $U$  is derived using a similar procedure. The inverse operator is given by the following expression,

$$\bar{P} = \bar{T}^{-1} * {}_2B * \tilde{T} * {}_0B^\dagger \bar{S} = \frac{1}{2} \bar{T}^\dagger * {}_2B * \tilde{T} * {}_0B^\dagger \bar{S} \quad (3.8)$$

$$= \bar{O}^{-1} * \bar{S} \quad (3.9)$$

We do not provide the explicit calculations here, since the real space inverse operator can be derived by contracting over all the matrix operators using a procedure nearly identical to that discussed in the previous section. The inverse operator is given by the following expression,

$$\bar{O}^{-1} = \begin{bmatrix} -\mathcal{M}_r & \mathcal{M}_i \\ -\mathcal{M}_i & -\mathcal{M}_r \end{bmatrix}_{2N_{\text{pix}} \times 2N_{\text{pix}}} = -f(\beta_{ij}, \ell_{\min}, \ell_{\max}) \begin{bmatrix} \cos(2\alpha_{ij}) & -\sin(2\alpha_{ij}) \\ \sin(2\alpha_{ij}) & \cos(2\alpha_{ij}) \end{bmatrix}, \quad (3.10)$$

where all the symbols have the same meaning as discussed in Sec. 3.1. Note that the kernel is different by a mere change in sign on the off-diagonals of the block matrix as compared to Eq. (3.6). We can evaluate the Stokes  $Q$  &  $U$  parameters from the scalar  $E$  &  $B$  fields by evaluating the following expression,

$$\begin{bmatrix} Q_i \\ U_i \end{bmatrix} = -f(\beta_{ij}) \begin{bmatrix} \cos(2\alpha_{ij}) & -\sin(2\alpha_{ij}) \\ \sin(2\alpha_{ij}) & \cos(2\alpha_{ij}) \end{bmatrix} \begin{bmatrix} E_j \\ B_j \end{bmatrix} \Delta\Omega, \quad (3.11)$$

where again the Einstein summation convention is implied and all the symbols have their usual meaning.

⇒ How does the radial kernel reduce to unity on evaluating the the operator on to its inverse ?

### 3.3 Decomposing Q & U Stokes parameters into those corresponding to E & B modes respectively

The Stokes Q & U parameters can be decomposed into the scalar modes E & B and vice versa, as seen in the previous sections. The E & B modes are orthogonal to each other. It is possible to decompose the Stokes Q & U parameters into those that purely contribute to E modes and those that purely contribute to the B mode of polarization. We can only measure the total Stokes parameters which is a sum of the Stokes Q & U corresponding to the respective scalar modes. In this section we derive the real space operators which directly decompose the total measured Stokes Q & U parameters to Stokes parameters corresponding to the scalar fields E & B respectively, *without ever having to evaluate the E & B modes explicitly*. Again the procedure is analogous to that discussed in Sec. 3.1, though the algebra is a little more involved. Here we use the harmonic space E/B projection operators  $\tilde{O}_{E/B}$ , defined in Eq. (2.12a), to derive the respective real space operators. It can be shown that the Stokes parameters corresponding to each scalar mode are given by the following expressions,

$$\begin{aligned}\bar{P}_E &= [\bar{T}^{-1} * {}_2B * \tilde{T} * \tilde{O}_E * \tilde{T}^{-1} * {}_2B^\dagger * \bar{T}] * \bar{P}, \\ &= [\frac{1}{4} \bar{T}^\dagger * {}_2B * \tilde{T} * \tilde{O}_E * \tilde{T}^\dagger * {}_2B^\dagger * \bar{T}] * \bar{P}, \\ &= \bar{O}_E * \bar{P},\end{aligned}\tag{3.12}$$

$$\begin{aligned}\bar{P}_B &= [\bar{T}^{-1} * {}_2B * \tilde{T} * \tilde{O}_B * \tilde{T}^{-1} * {}_2B^\dagger * \bar{T}] * \bar{P}, \\ &= [\frac{1}{4} \bar{T}^\dagger * {}_2B * \tilde{T} * \tilde{O}_B * \tilde{T}^\dagger * {}_2B^\dagger * \bar{T}] * \bar{P}, \\ &= \bar{O}_B * \bar{P}.\end{aligned}\tag{3.13}$$

We contract over all the matrix operators to arrive at the the real space operators. On simplification it can be shows that the real space operator takes up the following form,

$$\bar{O}_{E/B} = 0.5 \begin{bmatrix} \mathcal{I}_r \pm \mathcal{D}_r & -\mathcal{I}_i \pm \mathcal{D}_i \\ -\mathcal{I}_i \pm \mathcal{D}_i & \mathcal{I}_r \mp \mathcal{D}_r \end{bmatrix}_{2N_{pix} \times 2N_{pix}},\tag{3.14}$$

where  $\mathcal{I}_r$  &  $\mathcal{D}_r$  and  $\mathcal{I}_i$  &  $\mathcal{D}_i$  are the real and complex parts of the following complex functions,

$$\begin{aligned}\mathcal{I} &= \mathcal{I}_r + i\mathcal{I}_i = \sum_{\ell m} {}_2Y_{\ell m}(\hat{n}_i) {}_2Y_{\ell m}^*(\hat{n}_j), \\ \mathcal{D} &= \mathcal{D}_r + i\mathcal{D}_i = \sum_{\ell m} {}_2Y_{\ell m}(\hat{n}_i) {}_{-2}Y_{\ell m}^*(\hat{n}_j).\end{aligned}$$

These functions can be further simplified using the properties of spin spherical harmonics listed in Appendix 6.1. Specifically it can be shown that these functions reduce to the following mathematical forms,

$$\mathcal{I}(\hat{n}_i, \hat{n}_j) = \sum_{\ell} \sqrt{\frac{2\ell+1}{4\pi}} {}_2Y_{\ell-2}(\beta_{ij}, \alpha_{ij}) e^{-i2\gamma_{ij}} = \mathcal{I}_r + i\mathcal{I}_i,\tag{3.15a}$$

$$\mathcal{I}_r + i\mathcal{I}_i = \left[ \cos(2\alpha_{ij} + 2\gamma_{ij}) - i \sin(2\alpha_{ij} + 2\gamma_{ij}) \right] {}_{-2}f(\beta_{ij}, \ell_{min}, \ell_{max}),\tag{3.15b}$$

$$\mathcal{D}(\hat{n}_i, \hat{n}_j) = \sum_{\ell} \sqrt{\frac{2\ell+1}{4\pi}} {}_2Y_{\ell+2}(\beta_{ij}, \alpha_{ij}) e^{-i2\gamma_{ij}} = \mathcal{D}_r + i\mathcal{D}_i, \quad (3.16a)$$

$$\mathcal{D}_r + i\mathcal{D}_i = \left[ \cos(2\alpha_{ij} - 2\gamma_{ij}) + i \sin(2\alpha_{ij} - 2\gamma_{ij}) \right]_{+2} f(\beta_{ij}, \ell_{\min}, \ell_{\max}), \quad (3.16b)$$

where the functions,

$${}_{\pm 2}f(\beta, \ell_{\min}, \ell_{\max}) = \sum_{\ell=\ell_{\min}}^{\ell_{\max}} \sqrt{\frac{2\ell+1}{4\pi}} {}_{\pm 2}f_{\ell}(\beta), \quad (3.17)$$

can be expressed in terms of  $P_{\ell}^2$  Legendre polynomials and are given by the following explicit mathematical forms,

$$\begin{aligned} {}_{\pm 2}f_{\ell}(\beta) &= 2 \frac{(\ell-2)!}{(\ell+2)!} \sqrt{\frac{2\ell+1}{4\pi}} \left[ -P_{\ell}^2(\cos \beta) \left( \frac{\ell-4}{\sin^2 \beta} + \frac{1}{2}\ell(\ell-1) \pm \frac{2(\ell-1)\cos \beta}{\sin^2 \beta} \right) \right. \\ &\quad \left. + P_{\ell-1}^2(\cos \beta) \left( (\ell+2) \frac{\cos \beta}{\sin^2 \beta} \pm \frac{2(\ell+2)}{\sin^2 \beta} \right) \right]. \end{aligned} \quad (3.18)$$

Finally, the Stokes parameters corresponding to the respective scalar fields can be derived by evaluating the following expression,

$$\begin{aligned} \begin{bmatrix} Q_i \\ U_i \end{bmatrix}_{E/B} &= 0.5 \left\{ {}_{-2}f(\beta_{ij}, \ell_{\min}, \ell_{\max}) \begin{bmatrix} \cos(2\alpha_{ij} + 2\gamma_{ij}) & \sin(2\alpha_{ij} + 2\gamma_{ij}) \\ \sin(2\alpha_{ij} + 2\gamma_{ij}) & \cos(2\alpha_{ij} + 2\gamma_{ij}) \end{bmatrix} \begin{bmatrix} Q_j \\ U_j \end{bmatrix} \right. \\ &\quad \left. \pm {}_{+2}f(\beta_{ij}, \ell_{\min}, \ell_{\max}) \begin{bmatrix} \cos(2\alpha_{ij} - 2\gamma_{ij}) & -\sin(2\alpha_{ij} - 2\gamma_{ij}) \\ -\sin(2\alpha_{ij} - 2\gamma_{ij}) & -\cos(2\alpha_{ij} - 2\gamma_{ij}) \end{bmatrix} \begin{bmatrix} Q_j \\ U_j \end{bmatrix} \right\} \Delta\Omega, \end{aligned} \quad (3.19)$$

where all the symbols have their usual meaning.

### 3.4 Visualizing the convolution kernels

We begin by evaluating the functions  $f_{,+2} f$  &  $-_2 f$ . Since these functions determine the amplitude of the convolution kernels as a function of the angular distance  $\beta$  from the central pixel, we refer to them as the radial kernels. These functions have been calculated by evaluating the multipole sums in Eq. (3.5b) and Eq. (3.18) from  $\ell_{\min} = 2$  to  $\ell_{\max} = 96$ . The resultant functions are depicted in Fig. 1. Note that the function  $f(\beta)$ , which is a part of the real space convolution kernel which translates the coordinate dependent Stokes Q & U to coordinate independent scalars E & B, has a vanishing contribution from the location of the central pixel ( $\beta \rightarrow 0$ ). We recall that the fields E & B are scalar and hence immune

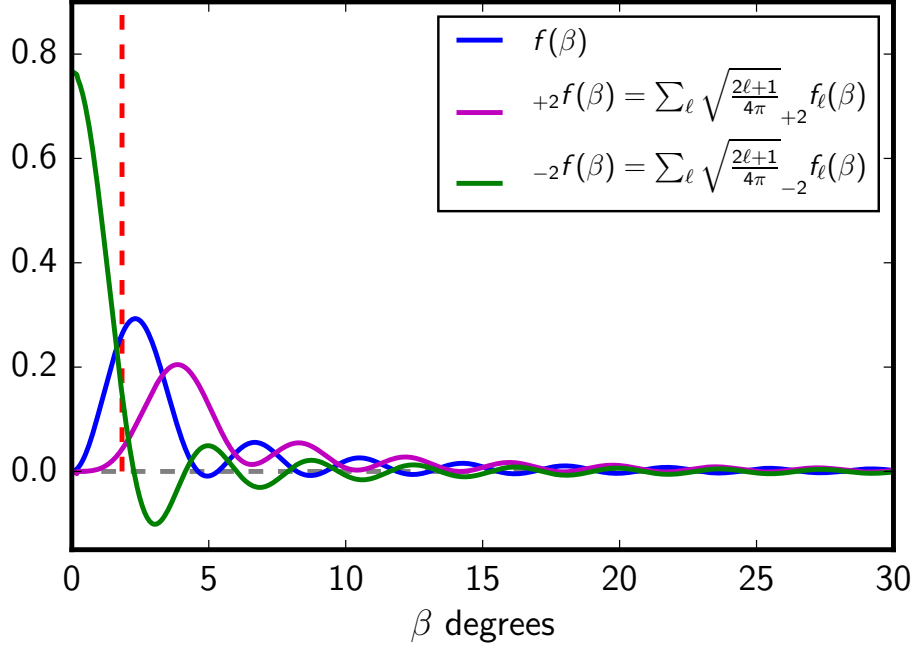


**Figure 1.** The figure depicts the radial part of the convolution kernels shown in Fig. 2. These radial function have been evaluated with the band limit fixed at  $\ell_{\max} = 96$ . The vertical dashed line marks the approximate size of a NSIDE=32 Healpix pixel.  $\Rightarrow$  [Update to Nside=64 ?](#)

to coordinate definitions. The locally defined Stokes parameters however necessarily depend on the coordinate definition. Therefore, this nature of the radial kernel is to be expected in order for it to satisfy the requirement of the derived quantities being scalars. The functions  $+_2 f(\beta)$  &  $-_2 f(\beta)$ , both contribute to the convolution kernels which decompose the Stokes parameters into those corresponding to the respective scalar modes E & B. Note that while  $-_2 f(\beta)$  specifically contributes at the location of the central pixel,  $+_2 f(\beta)$  dominates in the neighbouring regions which are approximately at least 1 pixel away from the central pixel.

In addition to the angular distance  $\beta$  from the central pixel, the convolution kernels also depend on the other Euler angles  $\alpha$  &  $\gamma$  as seen from Eq. (3.6), Eq. (3.15a) and Eq. (3.16a). We plot the real and imaginary parts of the functions  $\mathcal{M}$ ,  $\mathcal{D}$  &  $\mathcal{I}$  at different positions on the sphere. For illustration the functions have been sampled at a very high Healpix resolution parameter of NSIDE=2048. We evaluate parts of the convolution kernels at different locations on the sphere and the results are depicted in Fig. 2. **Since its not easy to imagine how the Euler angles vary as a function of position of the central pixel, we evaluate and depict the**

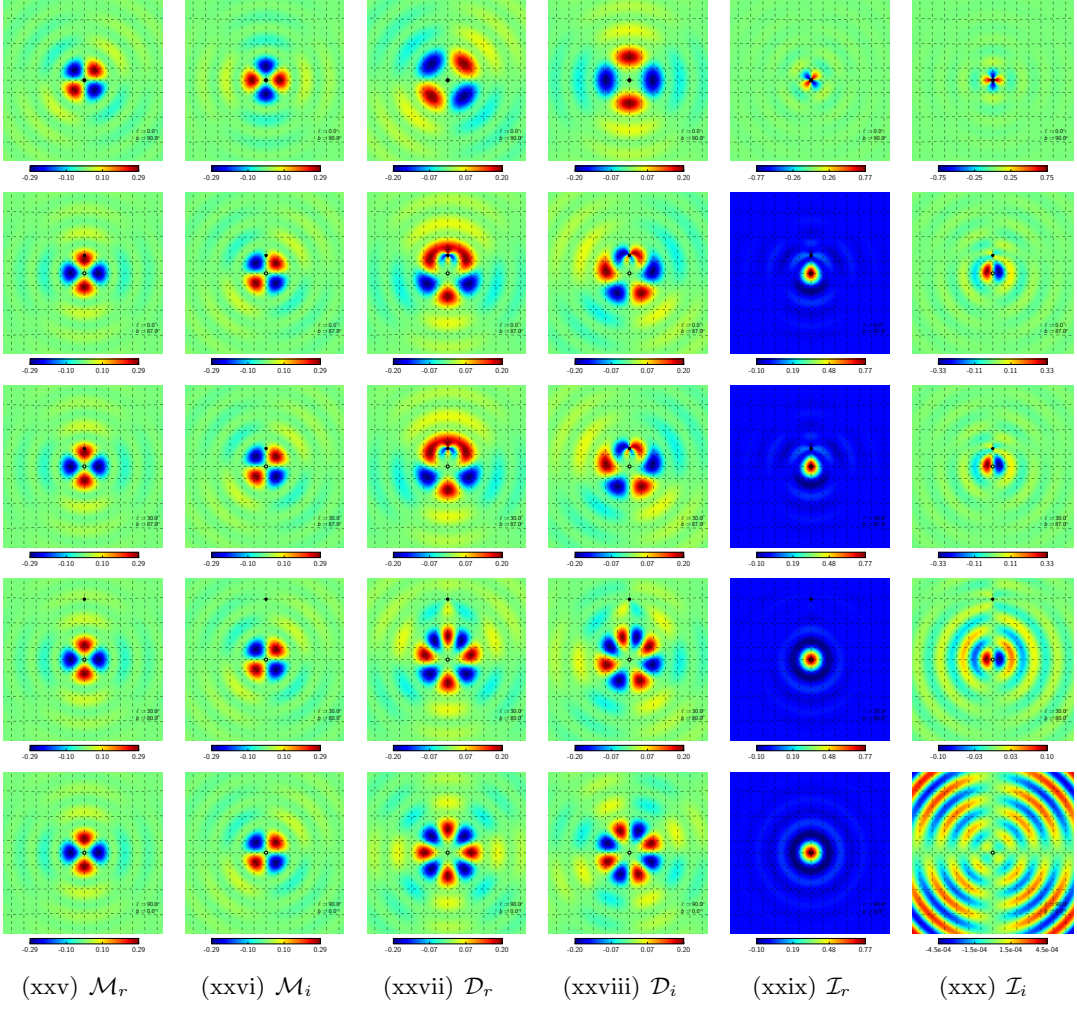


**Figure 2.** This panel of figure depicts the various parts of the convolution kernel, discussed in Sec. 3. These kernels have been evaluated with the band limit fixed at  $\ell_{\max} = 96$ , however the functions have been sampled at an NSIDE=2048 resolution for visual appeal. The size of each panel is approximately  $26^\circ \times 26^\circ$ . The black circles denotes the position of the central pixel around which the convolution kernels have been evaluated and the black star marks the location of the north galactic pole. The five rows depict the kernels at different location on the sphere and the galactic coordinates of the central pixel from top to bottom rows are as follows  $[b, \ell] = [0^\circ, 0^\circ], [87^\circ, 0^\circ], [87^\circ, 30^\circ], [80^\circ, 30^\circ], [0^\circ, 90^\circ]$ .

kernel at different locations on the sphere, to give a sense of how these kernels vary across the sphere. The function  $\mathcal{M}$  is nearly identical irrespective of changes in the galactic latitude and longitude of the central pixel. The only contrasting locations are the poles (i.e.  $|b| = 90^\circ$ ), where the functions  $\mathcal{M}_r$  &  $\mathcal{M}_i$  are rotated by  $45^\circ$  as compared to the respective functions evaluated at locations where  $|b| \neq 90^\circ$ . It is also important to note that these functions are not distorted when a part of the domain overlaps with the poles, as can be seen in the first four rows of Fig. 2. On the contrary, the function  $\mathcal{D}$  varies significantly as a function of galactic latitude of the central pixel. It varies from having a two fold symmetry at the poles to having a four fold symmetry at the equator as seen in the middle two columns of Fig. 2. This transformation arises from the distortions induced in this function as parts of

its domain passes the galactic poles. The function  $\mathcal{I}$  shows similar behavior, varying with latitude and being distorted in parts that overlap with the galactic poles. This function, in the ideal case of no band limit would reduce to a delta function at the position of the central pixel ( $\lim_{\ell_{\max} \rightarrow \infty} : \mathcal{I}_r \rightarrow \delta(\hat{n}_0 - \hat{n}')$ ,  $\mathcal{I}_i \rightarrow 0$ ), hints of which can be seen by comparing the amplitudes of the real and imaginary parts of this function in the last two columns of Fig. 2, especially close to the equator. Since we invariably work with a specific band limit, both the real and imaginary parts of this functions make important finite non-zero contributions. All the function are seen to be invariant under changes in longitude of the central pixel, the latitude being held fixed as can be seen by comparing the figures in the second (evaluated at  $[b, \ell] = [87^\circ, 0^\circ]$ ) and third row (evaluated at  $[b, \ell] = [87^\circ, 30^\circ]$ ) of Fig. 2, as one may have expected.

### 3.5 Quantifying the non-locality of E & B modes

It is clear that the non-locality of the E and B modes is determined by the radial part of the convolution kernels. To quantify this non-locality as a function of the resolution of the experiment, we evaluate only the radial part of the convolution kernel for different values of the maximum multipole  $\ell_{\max}$ , while keeping the lowest multipole fixed at  $\ell_{\min} = 2$ . The set of radial kernels so derived are plotted in Fig. 3. All the function have been normalized such that their global maxima is set to unity. Note that on increasing  $\ell_{\max}$  the radial kernels fall appear to shift left, becoming insignificant relative to their global maxima at progressively small angular distance  $\beta$  from the central pixel. We define the value of the abscissa at which the function  $f(\beta, \ell_{\min}, \ell_{\max})$  transits to being monotonously below 1% of the maxima of the function as the non-locality parameter:  $\beta_o$ . We find that the following empirical relation:  $\beta_o = \min(180, 180 \frac{24}{\ell_{\max}})$  can predict quite accurately the value of the non-locality parameter for a given maximum multipole  $\ell_{\max}$  and fixed  $\ell_{\min} = 2$ .

The envelope of the radial kernel  $f(\beta, \ell_{\min}, \ell_{\max})$  is observed to have a linear relation to the angular distance  $\beta$  in log space as seen in Fig. 3, indicating a power law fall off. A fit by eye indicates that the envelope of the function is well represented by a function proportional to  $\beta^{-1.5}$  in intermediate angular distance range. This is not valid in regions  $\beta \ll \beta_o$  and  $\beta \gg \beta_o$ , where the envelope of the function can be clearly seen to deviate from power law behavior (see Fig. 3).

⇒ There isn't too much of a discussion surrounding the function  $\pm f(\beta)$ . What do you want to say about these functions?

⇒ Do you want to comment on the telescoping behavior of these radial functions ?

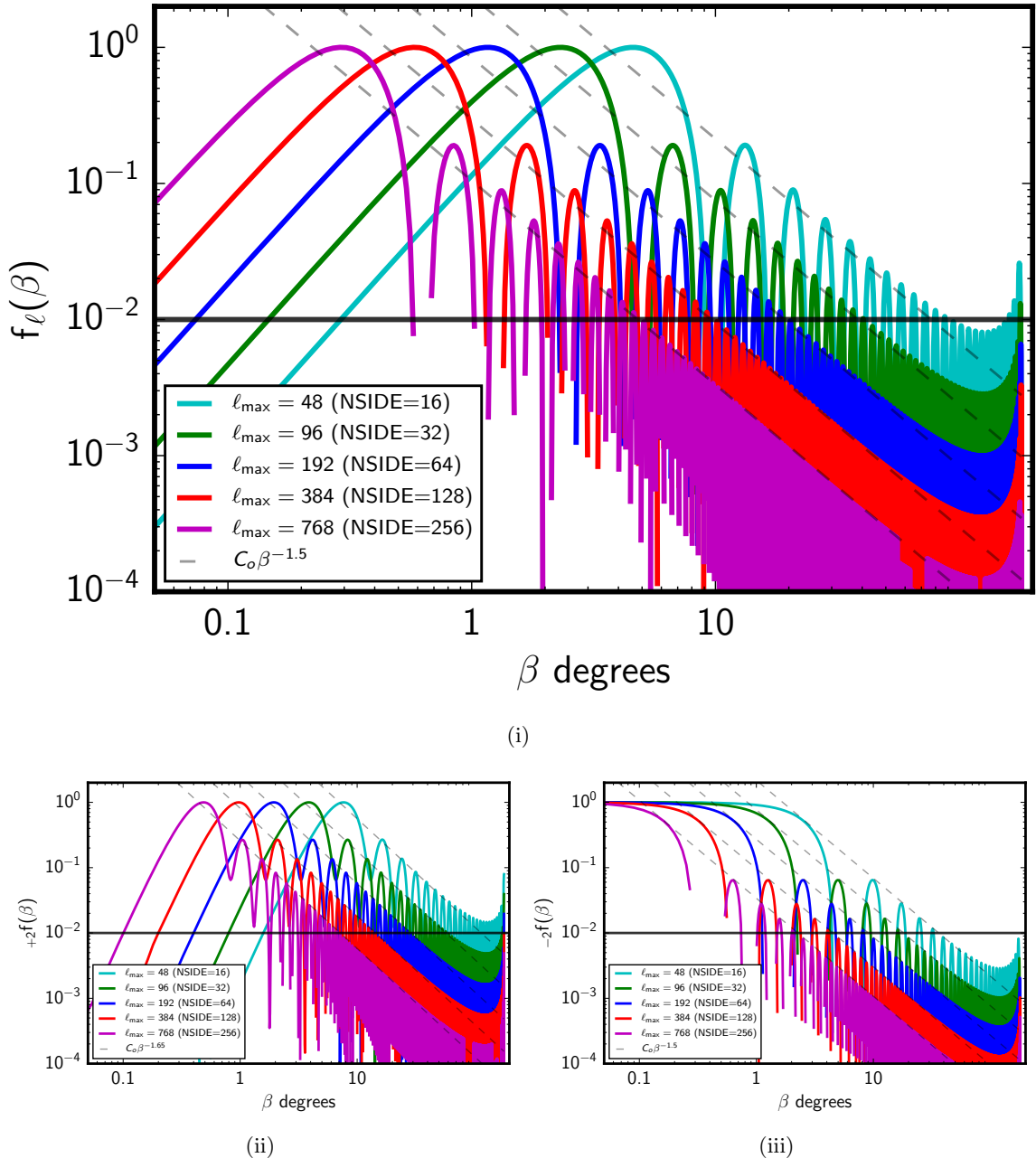


**Figure 3.** The top panel shows a plot of the radial kernels  $f(\beta, \ell_{\min}, \ell_{\max})$  while the bottom left and right panels show the radial functions  ${}_{+2}f(\beta, \ell_{\min}, \ell_{\max})$  &  ${}_{-2}f(\beta, \ell_{\min}, \ell_{\max})$  respectively, for different  $\ell_{\max}$  as indicated by the legends and fixed  $\ell_{\min} = 2$ . The curves for each of these functions have been normalized such that the maximum of the curve is set to unity. The horizontal solid black line marks the location where the amplitude of the kernel falls below 1% of its maximum. The slanted dashed black lines indicate a power law fit (by eye) to the envelope of the radial functions. While the envelopes for function  $f(\beta)$  &  ${}_{-2}f(\beta)$  are fit well by the power law  $\propto \beta^{-1.5}$ , the envelope for the function  ${}_{+2}f(\beta)$  is seen to have a slightly steeper fall off  $\propto \beta^{-1.65}$ .

## 4 Numerical implementation

As discussed in Sec. 3.5, the radial kernels decay ( $\propto \beta^{-1.5}$ ) as the distance from the central pixel increases, but they begin to increase on approaching the diametrically opposite position ( $\beta \rightarrow \pi$ ) as seen in Fig. 3. For a map containing sufficiently high multipole  $\ell_{\max}$  information, the local maxima the radial kernel attains in the vicinity of the diametrically opposite end is significantly smaller than global maxima. This suggests that for sufficiently high resolution CMB maps, it may suffice to restrict the convolution over the Stoke parameters Q & U to a local region around the central pixel. The size of this local region is determined by the non-locality parameter  $\beta_o$ . **It is important to note that this claim is valid only while working with maps that are fairly homogeneous.** In the case of foregrounds for example, though the radial kernel falls off, a strong foreground very far from the central pixel may still make significant contribution to the local definition of E and B modes.

In this section we study the effects of localizing the convolution kernels on the inferred E and B mode maps and their power spectra. We have developed a Python script to compute these local convolution over Stokes Q & U parameters. To carry out this numerical exercise, we pre-compute the radial part of the kernels, namely the function:  $f(\beta)$ ,  $+_2f(\beta)$  &  $-_2f(\beta)$ . We use the python routine `scipy.special.lpmn` for the numerical evaluation of the associated Legendre polynomial functions required to compute the respective radial kernels following equations Eq. (3.5b) and Eq. (3.17). Specifically while computing the functions  $+_2f(\beta)$  &  $-_2f(\beta)$  in the vicinity of  $\beta = 0$  &  $\pi$ , we use the limiting forms of the respective functions given in Appendix 6.2. As the next step, for each pixel on the Healpix map we get the pixel numbers of all the neighboring pixels lying within radius of  $r_{\text{cutoff}}$  from the central pixel using the Healpix routine `query_disc`. We then use the `pix2ang` function of Healpix to get the angular coordinates of the central  $(\theta_o, \phi_o)$  and its surrounding pixels  $(\theta_i, \phi_i)$ , which are used to calculate the corresponding Euler angles using Eq. (3.1a). Given these inputs we evaluate the convolutions as simple Reimann sums. We repeat this procedure for each pixel on the Healpix map to yielding the resultant maps (E, B, Q, U).

We use the CMB spectra for a fiducial cosmology and restrict our analysis on lensing induced B-mode spectra. For the results presented in the following sections we carry out our analysis on CMB maps at Healpix resolution of NSIDE = 64. In order to understand the effects of restricting the convolution to a local neighbourhood, we evaluate these convolutions on discs with progressively smaller radii surrounding the central pixel. Specifically the non-locality parameter for a NSIDE=64 map is  $\beta_o = 22.5^\circ$ . We impose radial cutoffs of  $r_{\text{cutoff}} = [2\beta_o, \beta_o, 0.5\beta_o, 0.25\beta_o]$  with an apodization of 3 degrees having a cosine squared profiles on the edges of the discs. We also evaluate the corresponding maps using standard full sky Healpix routines and use these as reference maps for this exercise. Note that the Healpix evaluations are equivalent to carrying out the convolutions over the full sphere (i.e.  $\beta_o = \pi$ ). We compare these maps to the reference maps and their respective spectra, to quantitatively understand the effect of the imposed radial cutoff on the convolutions.

### 4.1 Constructing E & B maps using local convolutions

Here we present the results of evaluating the local convolution given in Eq. (3.6), to derive E & B mode maps given maps of Stokes Q & U. The resultant maps are depicted in Fig. 4. Specifically the left column depicts the reference E & B maps derived using Healpix, the middle column depicts the E & B mode maps derived from local convolutions restricted to  $2\beta_o$  and difference between these maps is depicted in the right column. The differences between

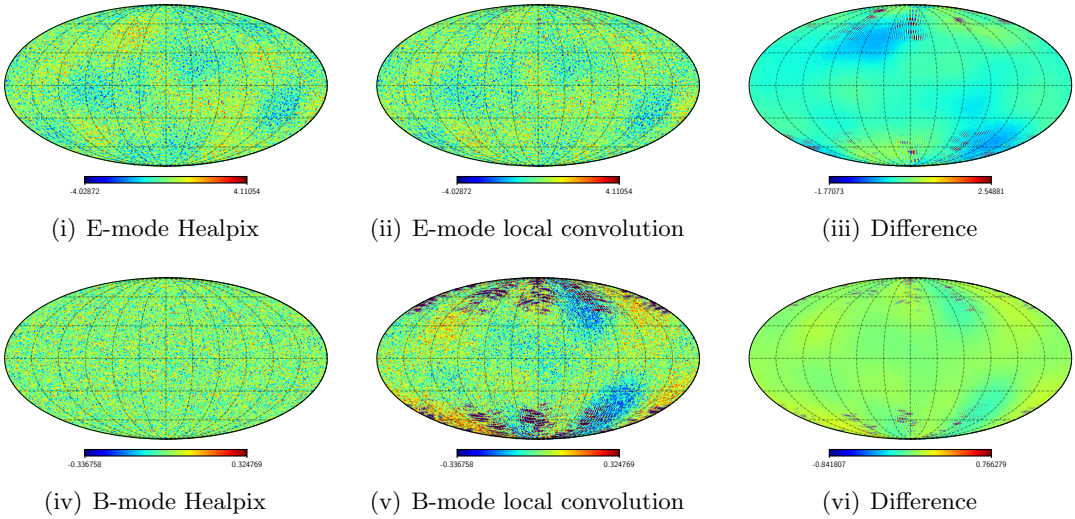


**Figure 4.** Left: Reference E & B mode maps derived using Healpix. Middle: E & B mode maps derived using  $r_{\text{cutoff}} = 2\beta_o$ . The color scale is saturated to that of the respective reference maps. Right: Difference between the maps shown in the left and middle columns.

these maps are observed to be large near the polar caps, however they are significantly smaller in the band around the equator. Further note that the differences seen around the equator are dominated by large scale modes, in contrast to the polar caps where one even observes small scale fluctuations.

Next we compute the power spectra of these local E & B maps and compare them to the spectra derived from the reference maps. The results of this exercise are summarized in Fig. 5. We note that when the radial cutoff is set much below the non-locality parameter as in  $r_{\text{cutoff}} = 0.25\beta_o$ , the spectra differ from the reference spectra by more than the cosmic variance. However on increasing the radial cutoff to only  $0.5\beta_o$ , the differences at most multipoles reduce to being comparable to the cosmic variance. On further increasing the radial cutoff to  $\beta_o$  and  $2\beta_o$ , the difference at most multipoles further reduce to levels of 0.5 cosmic variance or in absolute terms the differences are at the level of 2%. Also note that the improvement while transitioning from  $r_{\text{cutoff}} = \beta_o$  to  $r_{\text{cutoff}} = 2\beta_o$  are not as significant as seen while increasing the  $r_{\text{cutoff}}$  to  $\beta_o$ . This is can be understood as a consequence of the rapidly decaying nature of the radial kernels we discussed in Sec. 3.5.

At first glance, the above remarks seem to hold true only for the E mode spectra, since the errors in the B mode spectra seem to be significantly larger as seen in the middle row of Fig. 5. We understand that the higher error in the B mode spectra is primarily a combined effect of the low amplitude of the B mode spectrum as compared to the E mode spectrum and limited numerical accuracy of our simple convolution algorithm. We ran a number of tests to confirm these as reasons for the observed discrepant behaviour. We exchanged the E and B mode spectra, (taking care to set  $C_\ell^{TE} = 0$ ) and noted that the trends observed in the error plots are reversed, clearly indicating a dependence on the amplitude of the spectrum. We noted that the polar caps were particularly error prone, as seen in Fig. 4. We excised these error prone regions, specifically masking portions of the maps with  $|b| > 30^\circ$  to find that the errors on the B mode spectra revert to having very similar structure as that of the E mode spectra, as seen in the bottom row of Fig. 5. Finally we modify the use of standard

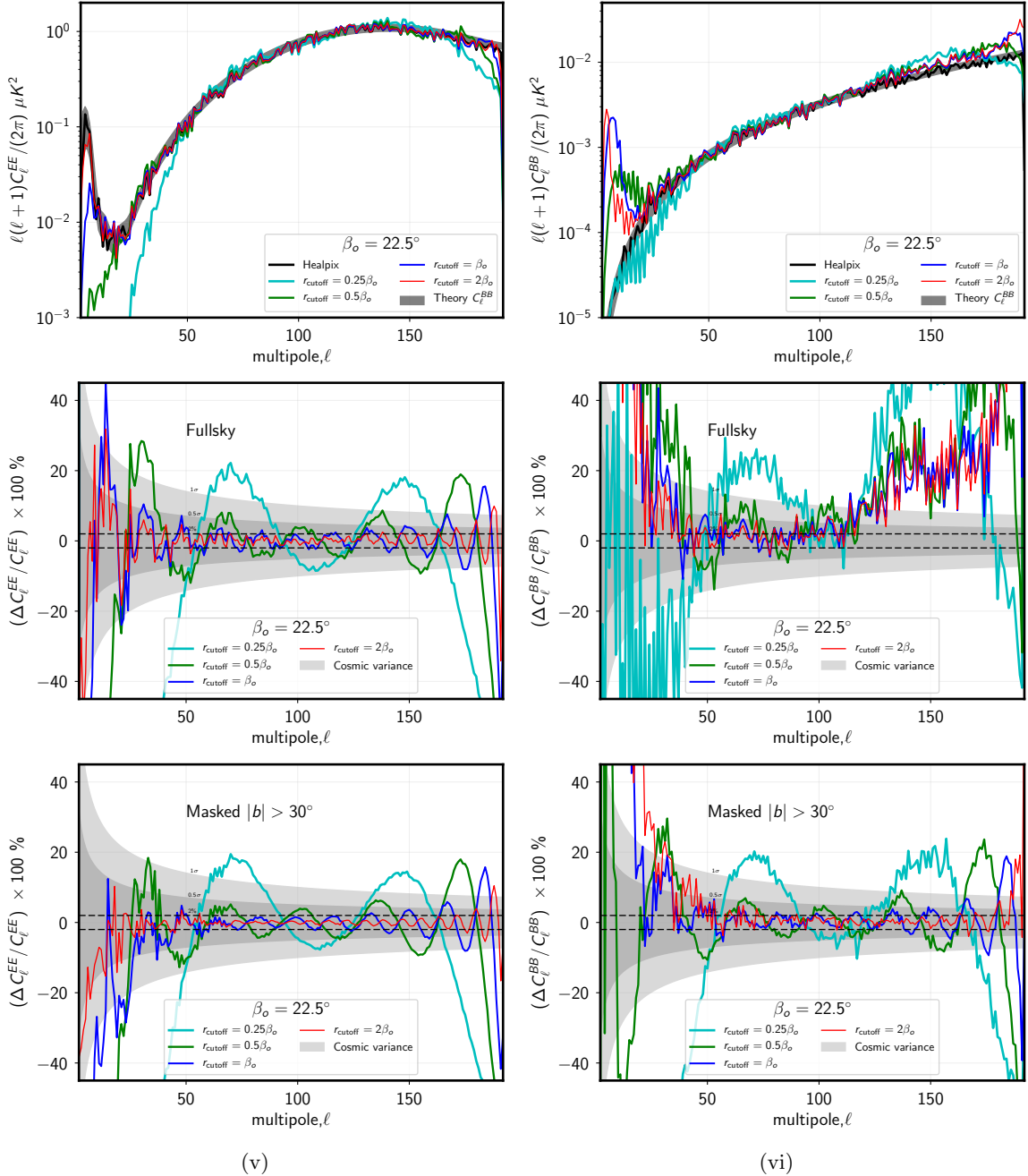


**Figure 5.** *Top:* The figures on left and right depict the E mode spectra and the B mode spectra respectively. *Middle:* These figures depict the relative percentage difference between the spectra derived from full sky, locally evaluated E & B maps and the reference spectra. *Bottom:* These figures depict the same results as shown in the middle row, except that the regions with  $|b| > 30^\circ$  of the maps have been masked for this analysis. The colors indicate the spectra derived from imposing different radial cutoff as indicated by the legends. The gray bands indicate the cosmic variance scatter around the fiducial spectra. The dashed horizontal black lines mark the 2% error.

Healpix routines to mimic the local convolution E & B construction (see Appendix 6.3 for details). The results from this exercise also concur with our understanding of the discrepant

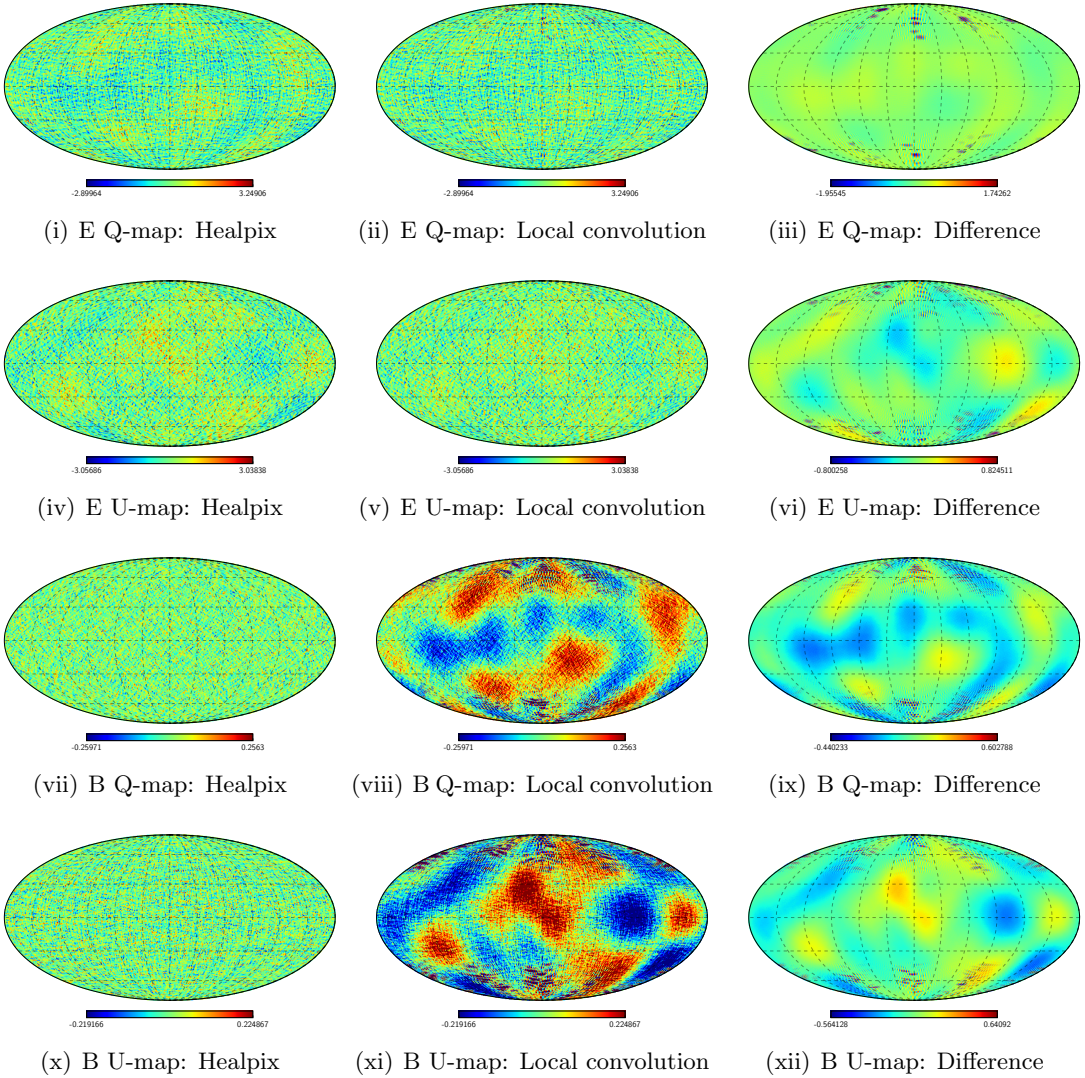


**Figure 6.** The top two rows depict the Stokes Q & U maps respectively corresponding to E mode of polarization while the bottom two rows depict the Stokes Q & U maps respectively corresponding to the B modes of polarization. *Left:* Stokes Maps derived using Healpix. *Middle:* Stokes maps derived using local convolution with  $r_{\text{cutoff}} = 2\beta_o$ . *Right:* Difference between the maps derived using the two different methods.

behaviour for the B-mode spectrum.

#### 4.2 Separating Stokes Q & U maps corresponding to E & B modes of polarization

In this section we present the results of evaluating the local convolution given in Eq. (3.19), to decompose the total Stokes Q and U parameters into those correspond to the E modes and B modes of polarization respectively. We reiterate that this procedure uses real space operation on the total Stokes Q and U maps and does not go through the process of constructing the E and B modes as is usually the case. The resultant Stokes Q and U maps corresponding to the E mode are depicted in the first two rows while those corresponding to B modes are

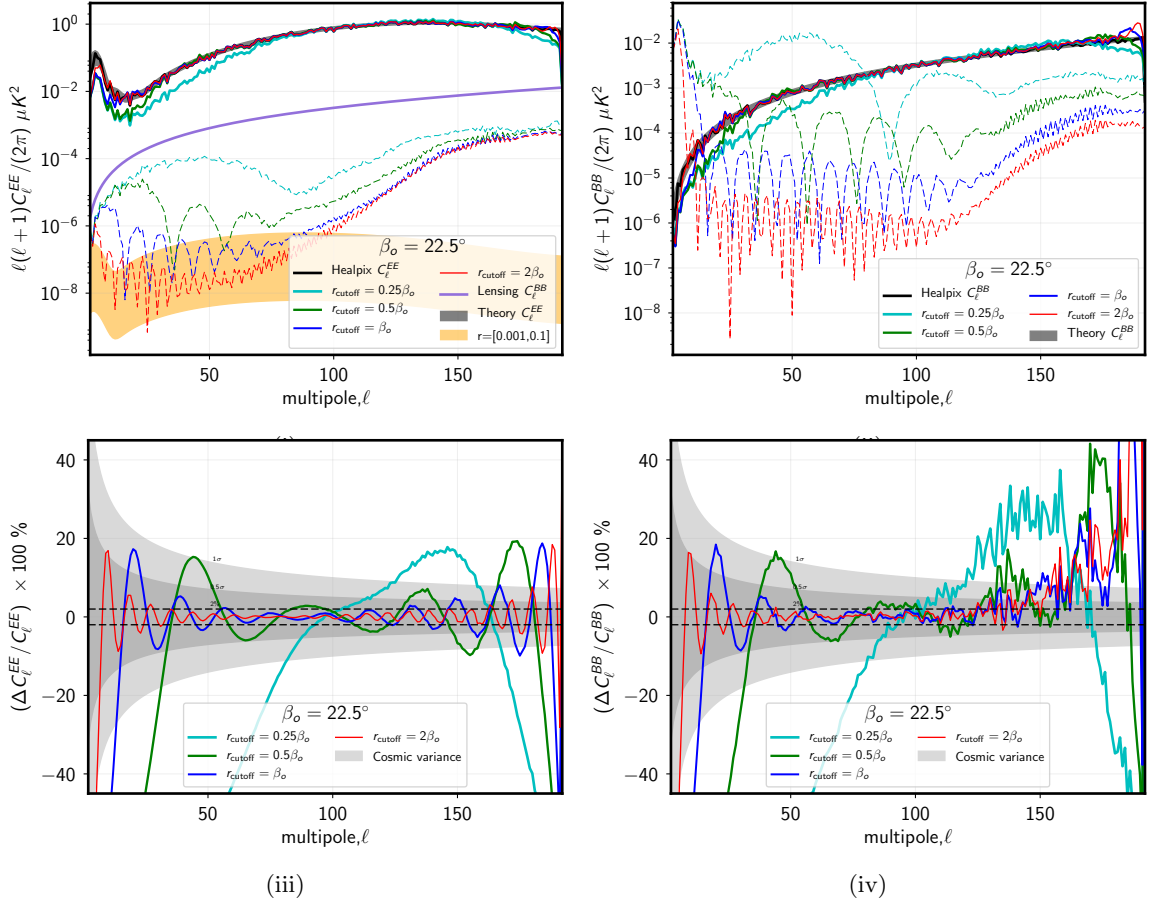


**Figure 7.** *Top:* The thick lines in the figure on left depicts the E mode spectra derived from pure E Stokes Q and U maps derived using different radial cutoffs, while the thin lines depict the residual B mode power. The figure on the right depict the same except that the thick lines now depict the B mode spectra while the thin lines show the residual E mode power. *Bottom:* The figure on the left and right depict the difference between the reference spectra and those derived from local convolution maps for different  $r_{\text{cutoff}}$  imposed on the convolution. In all the panels the color of the lines indicate the radial cutoff as indicated by the legend and the gray band marks the cosmic variance around the fiducial spectra.

shown in the final two rows of Fig. 6. The local convolution maps depicted in this figure are computed using a radial cutoff of  $r_{\text{cutoff}} = 2\beta_o$ . Note that similar to observations of the previous section, the maps derived via local real space convolutions, suffer from having relatively higher error in the polar caps, while the differences in the band around the equator are smaller and dominated by large scale modes. Next we compute the E and B mode spectra from the set of Stokes maps constructed using local convolutions with different  $r_{\text{cutoff}}$ . Note that for this exercise we use the standard Healpix routines for computing the spectra from the Stokes maps. The spectra derived from these local convolution maps and their difference with respect to the reference spectra are depicted in Fig. 7. The observations are similar to that made in the previous section: the difference with respect to the reference spectra reduce on increasing the radial cutoff and reach 2% levels at most multipoles for the maximum radial  $r_{\text{cutoff}} = 2\beta_o$  used in this analysis. In particular here we note that the B-mode residue

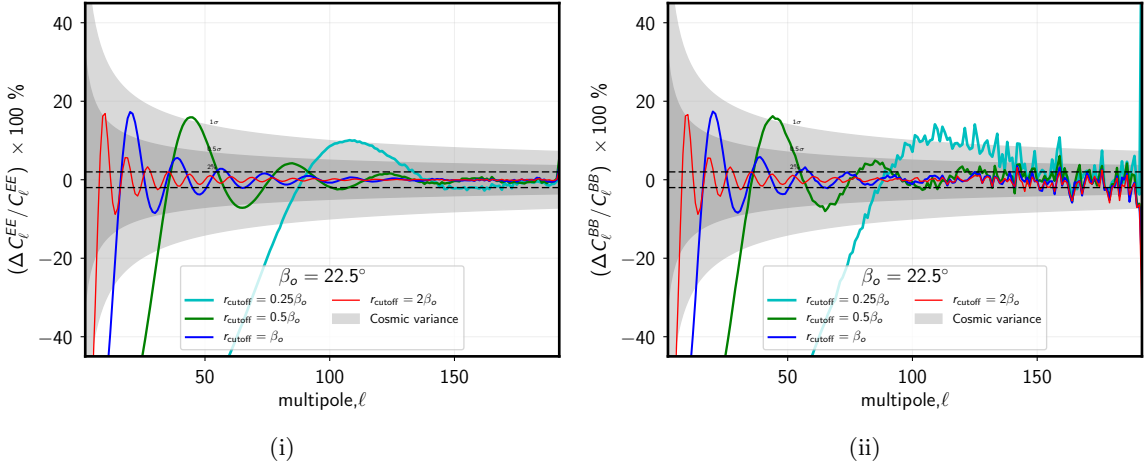


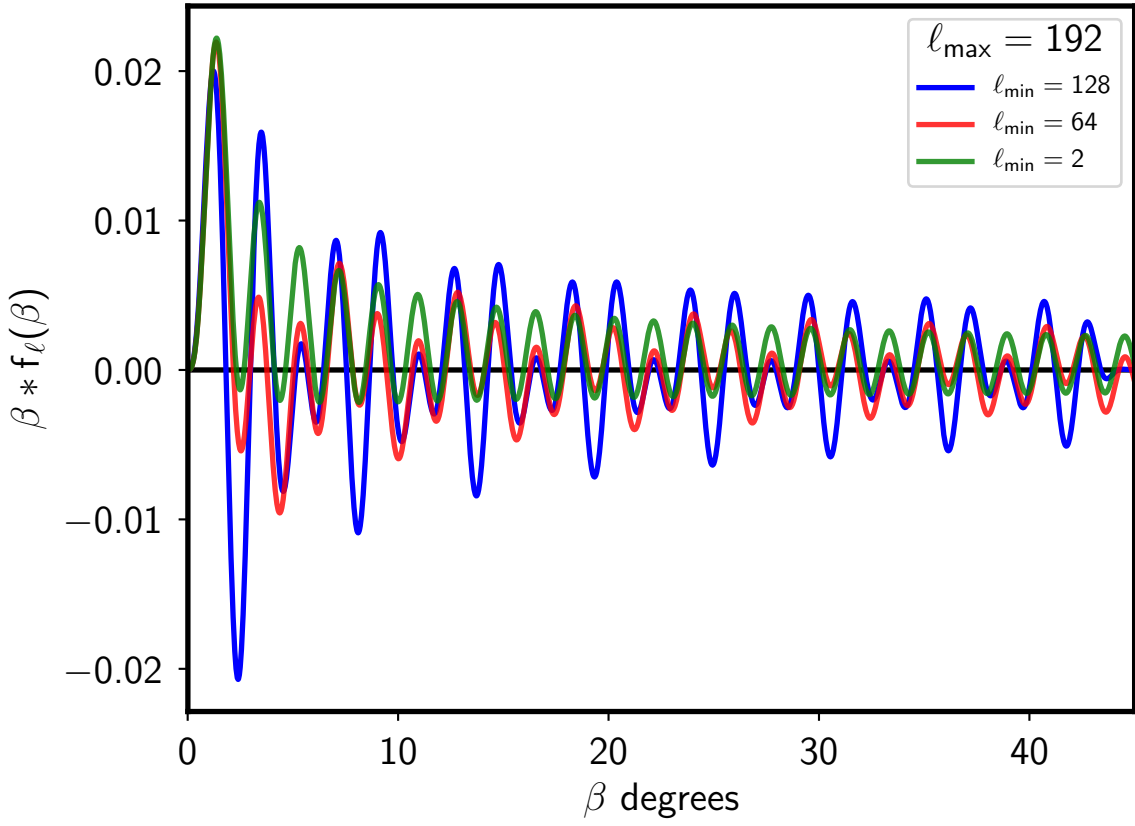
**Figure 8.** This figure depicts the same as the bottom panel of Fig. 7. The Stokes Q and U maps corresponding to E and B modes used in this analysis are constructed using the following relations:  $[Q, U]_E = [Q, U] - [Q, U]_{Local}^B$ ;  $[Q, U]_B = [Q, U] - [Q, U]_{Local}^E$ .

in the Stokes Q & U maps corresponding to E-modes is much smaller as compared to the E-mode residue in the Stokes Q & U maps computed for the B-modes of polarization. At all multipoles the B-mode residual power is below the lensing B-modes. The E-mode residual power at low multipoles is almost fully intact.

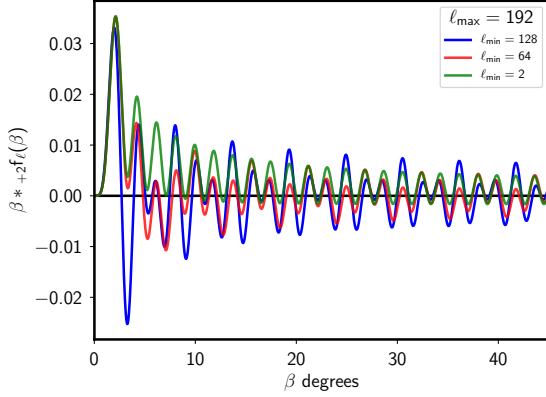
Motivated by these observations we also compute the Stokes Q & U maps corresponding to B-modes of polarization by simply subtracting the Stokes Q & U maps corresponding to E-mode from the total Stokes Q & U maps. For completeness we also compute the Stokes Q & U maps corresponding to E-mode in an analogous manner. We carry out a spectral study on these Stokes Q & U maps corresponding to E & B modes, computed using this alternate method. The results of the spectral analysis are summarized in Fig. 8. We observe that the the low multipole spectral behavior is not affected by this alternate construction of pure Stokes Q & U maps. The high multipole behavior is significantly altered as can be seen by comparing Fig. 8 with lower panels of Fig. 7. The relative percentage difference with respect to the reference spectra is seen to lie well within 2% error for sufficiently high multipoles for all radial cutoff  $r_{\text{cutoff}}$ .

### 4.3 Multipole filtering using spatial convolutions

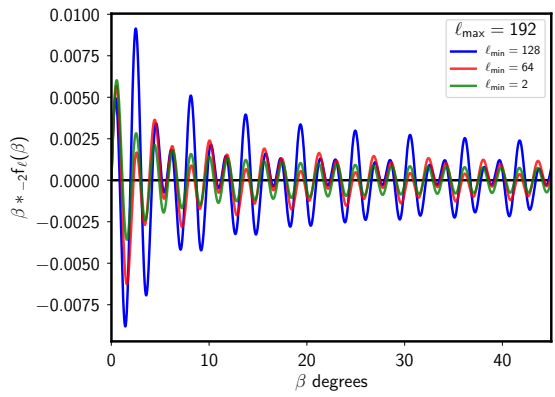
In this section we construct radial kernels which result in the desired multipole filtering, which can be achieved by simply controlling the  $\ell_{\min}$  &  $\ell_{\max}$  arguments of the functions  $f(\beta, \ell_{\min}, \ell_{\max})$  and  $\pm_2 f(\beta, \ell_{\min}, \ell_{\max})$ . We reiterate that only the radial part of the convolution kernel encodes the multipole information, while the azimuthal part of the kernel is independent of multipoles. As seen in the previous sections, using local convolution methods to separate E and B modes does not allow the recovery of large scale modes. This can be understood as occurring due to the following reason: localizing the convolution kernel by introducing a radial cut off, progressively reduces the overlap of the kernels for pixels on increasing the separation between them. The overlap begins to significantly drop when angular distances are larger than  $r_{\text{cutoff}}$  and reaches a null at a separation of  $2r_{\text{cutoff}}$ . Owing to this overlap reduction, the pixels at large separation in the constructed maps have a re-



(i)



(ii)



(iii)

**Figure 9.** This figure depicts the all the radial kernels evaluated for different multipole filters. In the filtered kernels presented here, only  $\ell_{\min}$  has been altered while the maximum multipole is held fixed at  $\ell_{\max} = 192$ . The kernels have been multiplied by a factor of the argument  $\beta$  to highlight the differences in the kernel at large angular separations  $\beta$ .

duced correlation, specifically  $C(\theta > 2r_{\text{cutoff}}) = 0$ . This motivates the construction of high pass filters especially while working with local convolution maps.  $\Rightarrow$  This should results in systematically lower power on large angular scales. This is observed for E mode spectra, but

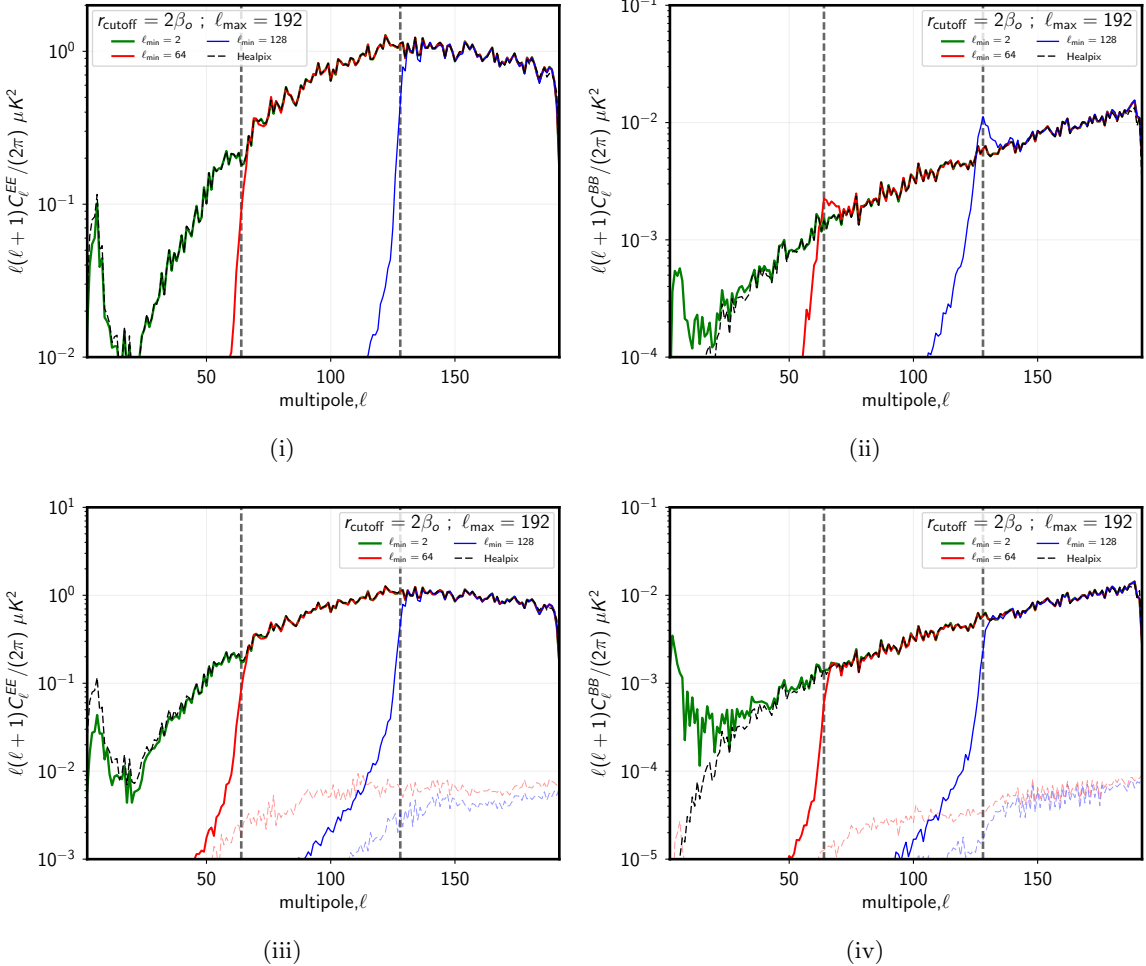


**Figure 10.** The top left and right panels depict the spectra for E and B modes respectively, where each panel shows the spectra derived from filtered E & B maps computed using local convolutions. The bottom left and right panels depict the same for spectra derived from  $[Q, U]_E$  and  $[Q, U]_B$  maps computed using local convolutions. The thin dashed lines in the bottom panels depict the residual power in the orthogonal modes. The vertical gray lines mark the low multipole cut off corresponding to  $\ell_{min} = 64$  and  $\ell_{min} = 128$ . All local convolution have been performed with  $r_{cutoff} = 2\beta_o$ .

not quiet for B. Why is that ?. We construct radial filters with three different low multipole cut-offs:  $\ell_{min} = 2, 64 \& 128$  which are depicted in Fig. 9. The kernels have been purposefully multiplied by a factor of the angular distance  $\beta$  to highlight the differences in the radial kernels for different multipole cut-offs.

We use these different radial kernels to perform local convolutions on the simulated polarization maps. We use the same radial cut off:  $r_{cutoff} = 2\beta_o$  for all the different filters, where  $\beta_o = 22.5^\circ$ . The spectra from the filtered maps so constructed are depicted in Fig. 10. Through these results we demonstrate how we can alter the radial part of the convolution kernels to get maps with the desired multipole filtering.  $\Rightarrow$  What do you have to say about the jump in power for the B mode spectra at the low multipole cutoff, derived from filtered B maps ?

#### 4.4 Application to Planck 353 Ghz polarization maps

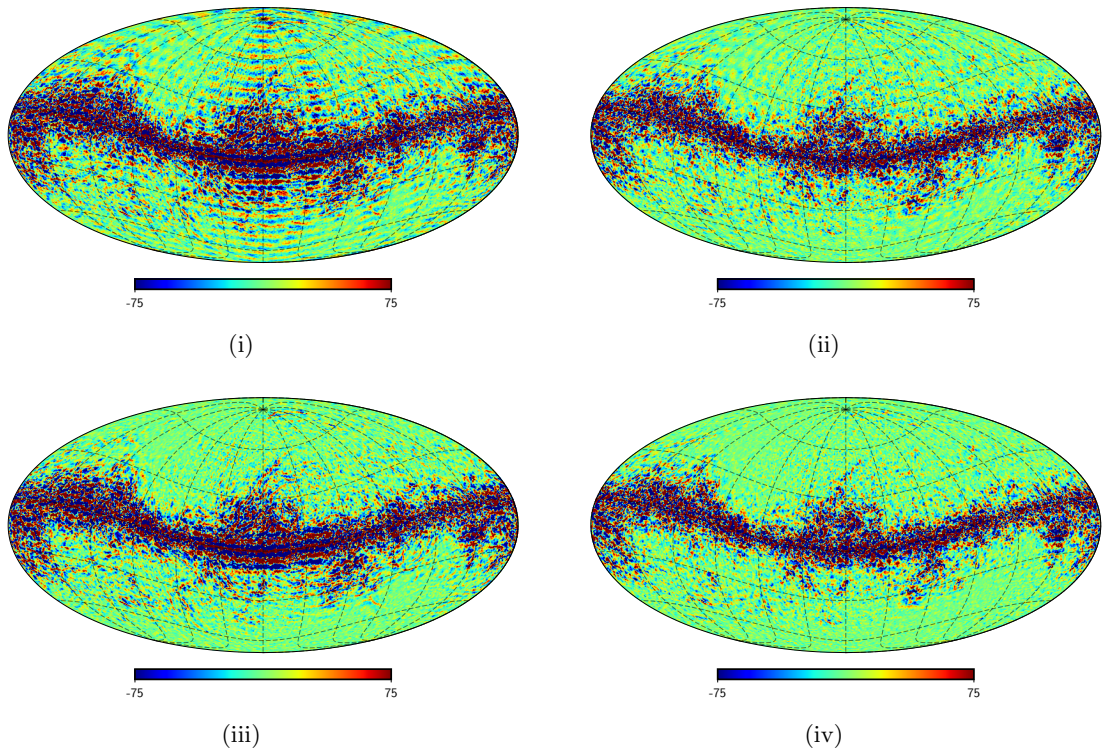
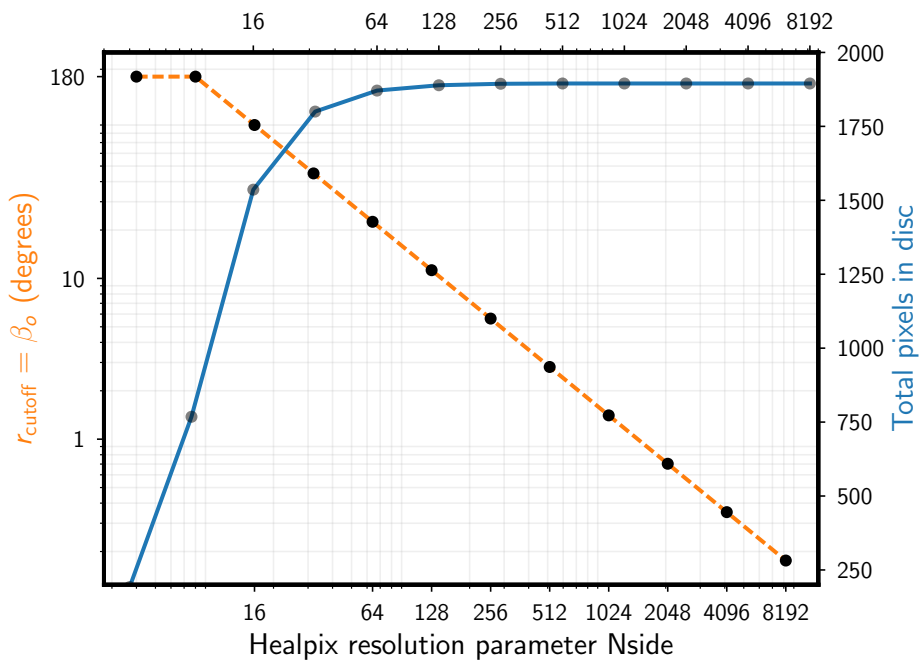


**Figure 11.**

#### 4.5 Scaling and future prospects



(i)

**Figure 12.** The red dashed curve depicts the how  $\beta_o$  changes as a function of the Healpix resolution parameter  $N_{\text{side}}$  assuming that the maximum multipole accessible in the map is given by  $\ell_{\max} = 3 * N_{\text{side}}$ . The blue solid curve depicts the number of surrounding pixel that will need to be accessed to carry out the convolution on Stokes Q & U maps to infer the value of the scalar fields E & B at the central pixel.

## 5 Discussion

- Many CMB experiments cannot access the large angle modes due to limited sky coverage. Often the large angle analysis is deal with in pixel space owing to the non-Gaussianity of the likelihood functions. With all these as motivations we study how the radial filters are modified by removing the large scale modes. We try to understand how removing large scale modes effects the locality of the E and B map estimators. We demonstrate that it is possible to get filtered maps by using the modifying the radial filter.
- We have derived the real space kernels for translating Stokes parameters Q & U to scalars E & B and vice versa. We have also derived real space kernels which allow for direct separation of Stokes Q & U parameters without having to first evaluate the scalar field E & B.
- These kernels quantify the non-locality of the E and B fields. We have introduced the non-locality parameter  $\beta_0$  which provides a quantitative measure of the non-locality of these fields.
- Studying these real space kernels reveals that its the radial part of the kernel which knows about the band limit of the experiment. Motivation for defining radially compact kernels. We have demonstrated that using the radially compact kernels does not bias the spectral information on intermediate angular scales.
- Small field experiments like BICEP implement such radial cut offs due to limited survey area.
- Using in conjunction with FEBECOP [5] like schemes to directly infer E and B mode maps from raw maps.
- *Total convolution methods:* Since the convolution kernels can be thought of as effective beams for polarization maps, it may be possible to use total convolution methods to construct E and B mode maps.
- Separate Q and U maps for E and B: We have presented kernels which allow for decomposition of the total Stokes Q and U parameters to those corresponding to E and B modes. This could be potentially interesting, since one can now work with E and B modes foregrounds and their separations separately.  $\Rightarrow$  **But is there an issue with doing this in the standard method which involves going through the process of generating E and B modes ?**
- *Mask leakages* can be understood as arising from improper sine quadrupole and cosine quadrupole transforms on rings with holes in them due to masking. For the global mask (no point sources), by using a radially compact kernel with some  $\beta_0$ , the pixels which are at a angular distance  $\beta_0$  from the edges of the mask have unbiased estimates of the scalar fields E and B.
- The difference between the spectra derived from the local convolution maps and the reference spectra follow a definite pattern and maybe it possible to model this difference and correct for it. For this purpose one will have to model the two point correlation function for the E and B fields in terms of the Stokes Q and U maps.

- Poor sensitivity to large scale modes as the local estimated maps do no carry information from pixel which are further away than the radial cutoff. This should cause a compromise on spectral estimates of low multipoles, which correspond to large angular scales, much larger than radial cutoff.
- We have not addressed the E to B leakage issue in this work.

## 6 Appendix

### 6.1 Mathematical properties of spin spherical harmonics

The sum over  $m$  index of product of two spherical harmonic functions of spin  $s_1$  and  $s_2$  respectively, is given by the following expression [4],

$$\sum_m {}_{s_1}Y_{\ell m}^*(\hat{n}_i) {}_{s_2}Y_{\ell m}(\hat{n}_j) = \sqrt{\frac{2\ell+1}{4\pi}} {}_{s_2}Y_\ell^{-s_1}(\beta, \alpha)e^{-is_2\gamma}, \quad (6.1)$$

where  $\alpha$ ,  $\beta$  &  $\gamma$  correspond to the Euler angles that specify the rotation matrix which transforms the local cartesian coordinates defined at  $\hat{n}_i$  such that it aligns with the local cartesian coordinate system at  $\hat{n}_j$ .

The spin spherical harmonics satisfy the following orthogonality relations,

$$\int {}_s Y_{\ell m}(\hat{n}) {}_s Y_{\ell' m'}^*(\hat{n}) d\Omega = \delta_{\ell\ell'} \delta_{mm'}, \quad (6.2)$$

where  $s$  denotes the spin of the spherical harmonic coefficients. The numerical validity of Eq. (6.2) is only limited by the rate at which these functions are sampled on the sphere and hence this identity can be made arbitrarily accurate by choosing a sufficiently high sampling rate.

The spin spherical harmonic functions satisfy the following completeness relation,

$$\sum_{\ell m} {}_s Y_{\ell m}(\hat{n}_i) {}_s Y_{\ell m}^*(\hat{n}_j) = \delta(\hat{n}_i - \hat{n}_j), \quad (6.3)$$

Note that the numerical validity of Eq. (6.4) is strictly true only when the sums over the indices  $(\ell, m)$  run to infinity. This is never true in practice, since the measured data invariable are band limited owing to the finite resolution of the experiments. Hence this relation is only approximately true and in more realistic scenario takes up the following function form,

$$\begin{aligned} \sum_{\ell=\ell_{\min}, m}^{\ell_{\max}} {}_s Y_{\ell m}(\hat{n}_i) {}_s Y_{\ell m}^*(\hat{n}_j) &\approx \delta(\hat{n}_i - \hat{n}_j), \\ &= \sum_{\ell=\ell_{\min}}^{\ell_{\max}} \sqrt{\frac{2\ell+1}{4\pi}} {}_s Y_\ell^{-s}(\beta, \alpha)e^{-is\gamma}, \end{aligned} \quad (6.4)$$

where  $\alpha$ ,  $\beta$  &  $\gamma$  are the Euler angles relating the two directions  $\hat{n}_i$  and  $\hat{n}_j$ . A specific case of this function with  $(s = 2, \ell_{\min} = 2, \ell_{\max} = 96)$  is depicted in the last two columns of Fig. 2.

### 6.2 Asymptotic forms for the functions $\pm {}_2 f_\ell(\beta)$

The functions  $\pm {}_2 f_\ell(\beta)$  need to be evaluated close to  $\beta = 0$  and  $\beta = \pi$ . Close to these values we cannot evaluate these functions using the relation given in Eq. (3.18), owing to the inverse  $\sin(\beta)$  dependence of a number of terms. To overcome this issue, we use the asymptotic form of the Legendre polynomials as  $\beta \rightarrow 0$ ,

$$P_\ell^2(\cos \beta) = \sin^2(\beta) \frac{(\ell+2)!}{8(\ell-2)!}. \quad (6.5)$$

Using the above limiting form, the functions  $\pm f_\ell(\beta)$  reduce to the following equations,

$$\lim_{\beta \rightarrow 0} \pm f_\ell(\beta) = \frac{1}{4} \sqrt{\frac{2\ell+1}{4\pi}} \left\{ - \left[ (\ell-4) + \frac{1}{2}\ell(\ell-1) \sin^2(\beta) \pm 2(\ell-1) \cos(\beta) \right] \right. \\ \left. + [(\ell-2) \cos(\beta) \pm 2(\ell-2)] \right\}. \quad (6.6)$$

Using the parity property of the associate Legendre polynomials:  $P_\ell^m(-x) = (-1)^{\ell+m} P_\ell^m(x)$ , the asymptotic form for the functions  $\pm f_\ell(\beta)$  in the limit  $\beta \rightarrow \pi$  are given by the following equations,

$$\lim_{\beta \rightarrow \pi} \pm f_\ell(\beta) = \frac{1}{4} \sqrt{\frac{2\ell+1}{4\pi}} \left\{ - \left[ (\ell-4) + \frac{1}{2}\ell(\ell-1) \sin^2(\beta) \pm 2(\ell-1) \cos(\beta) \right] (-1)^\ell \right. \\ \left. + [(\ell-2) \cos(\beta) \pm 2(\ell-2)] (-1)^{\ell-1} \right\}. \quad (6.7)$$

We use these asymptotic forms for  $\pm f_\ell(\beta)$  to evaluate the radial kernel close to the poles.

### 6.3 Convolution error

Here we assess error in the simple integeration scheme used in our python script. To estimate the error, we use the Healpix integration scheme as the reference. The spatially local convolutions suggested in this work can be carried out using Healpix via the following algorithm: (i) Generate a disc mask of radius  $r_{\text{cutoff}}$  around a pixel with index “i”. (ii) Apply the mask on the Stokes Q & U maps and evaluate the E & B maps using standard Healpix functions. (iii) Store the E & B field values evaluated at the pixel with index “i” (the center of the disc mask), while rejecting the fields constructed at other pixels in the mask. (iv) Repeat this process at all pixels to generate a map of the scalar fields E & B. This scheme is mathematical identical to our implementation of carrying out the convolution integrals over spatially local regions. In the above proposed algorithm the locality is enforced by the disc mask. However note that evaluating this scheme using Healpix is extremely inefficient since it effectively involves translating Npix Stokes Q & U maps to scalar E & B maps. The computational cost of carrying out this operation using Healpix grows quickly with the resolution parameter Nside. For the results presented here we work with Healpix maps simulated at a resolution of Nside=64.

We evaluate the E & B maps using three different methods, using our simple Python implementation of the local convolutions, the equivalent scheme using Healpix as described above and the full sky Healpix evaluation (which we use to evaluate the reference spectra). The relative percentage differences between the spectra derived from maps using the local methods and the reference spectra are depicted in Fig. 13. Note that the error on the E mode spectrum derived from maps constructed using the two different local convolution methods nearly match each other. However for the B-mode spectrum, the error on the spectrum derived from our python implementation is significantly larger as compared to the error on the spectrum derived from the local Healpix convolution method. This indicated the fact that Healpix convolution has a better accuracy as compared our implementation. More important to note here is the fact that the error on the spectra from locally evaluated E and B mode maps are nearly equal to each other, as can be seen by comparing the green curves in the left and and right panels of Fig. 13.

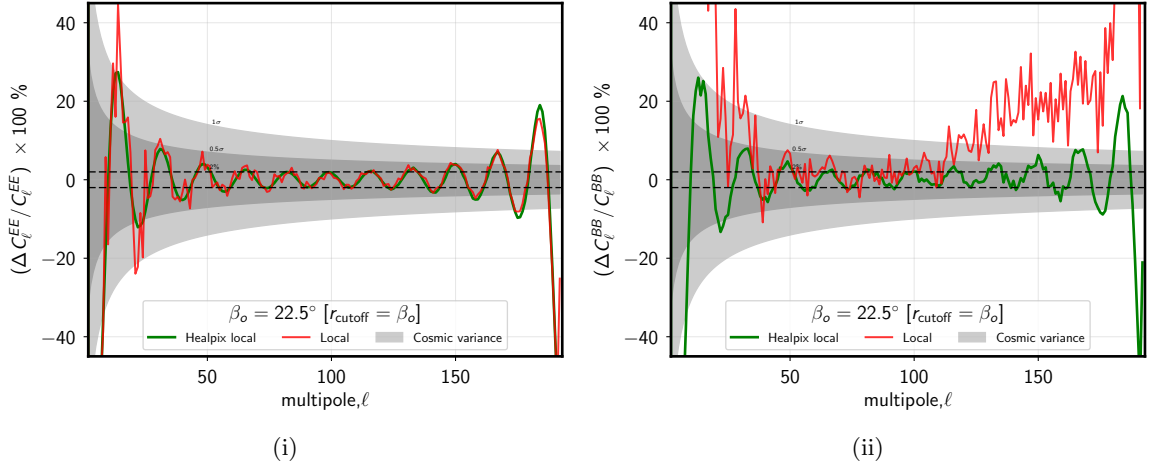


**Figure 13.** The figure on the left and right depict the relative percentage difference between spectra derived from local convolution estimates of E & B map and the reference spectra derived from full sky Healpix evaluations. The green curves depict the results from local E & B maps evaluated using local Healpix operations while the red curve shows the same for the scalar maps derived using our python script. The gray band indicates the scatter expected due to cosmic variance, the lighter shade corresponding to  $1\sigma$  and the darker shade to  $0.5\sigma$ . **The cosmic variance band does not account for the non-gaussian distribution, which is particularly relevant at the low multipoles.**

## 6.4 The correlation function and radial cut offs.

## References

- [1] M. Zaldarriaga, *The nature of the E-B decomposition of CMB polarization*, *Phys. Rev. D* **64** (jun, 2001) 103001, [[0106174](#)].
- [2] M. Kamionkowski, A. Kosowsky and A. Stebbins, *Statistics of cosmic microwave background polarization*, *Phys. Rev. D* **55** (1997) 7368–7388, [[9611125](#)].
- [3] J. N. Goldberg, A. J. Macfarlane, E. T. Newman, F. Rohrlich and E. C. G. Sudarshan, *Spin-s Spherical Harmonics and \eth*, *J. Math. Phys.* **8** (nov, 1967) 2155.
- [4] D. A. Varshalovich, A. N. Moskalev and V. K. Khersonskii, *Quantum Theory of Angular Momentum* (World Scientific). World Scientific, 1988.
- [5] S. Mitra, G. Rocha, K. M. Górski, K. M. Huffenberger, H. K. Eriksen, M. a. J. Ashdown et al., *FAST PIXEL SPACE CONVOLUTION FOR COSMIC MICROWAVE BACKGROUND SURVEYS WITH ASYMMETRIC BEAMS AND COMPLEX SCAN STRATEGIES: FEBECoP*, *Astrophys. J. Suppl. Ser.* **193** (mar, 2011) 5, [[1005.1929](#)].